

See discussions, stats, and author profiles for this publication at: <https://www.researchgate.net/publication/45800569>

# Properties of non-IPR fullerene films versus size of the building blocks

ARTICLE *in* PHYSICAL CHEMISTRY CHEMICAL PHYSICS · SEPTEMBER 2010

Impact Factor: 4.49 · DOI: 10.1039/c0cp00137f · Source: PubMed

CITATIONS

15

READS

40

6 AUTHORS, INCLUDING:



**Seyithan Ulas**

Karlsruhe Institute of Technology

8 PUBLICATIONS 30 CITATIONS

SEE PROFILE



**Stefan-Sven Jester**

University of Bonn

45 PUBLICATIONS 384 CITATIONS

SEE PROFILE



**Patrick J Weis**

Mercy Hospital Springfield MO

78 PUBLICATIONS 2,395 CITATIONS

SEE PROFILE



**Artur Böttcher**

Karlsruhe Institute of Technology

93 PUBLICATIONS 1,228 CITATIONS

SEE PROFILE

# Properties of non-IPR fullerene films *versus* size of the building blocks

Daniel Löffler,<sup>†a</sup> Seyithan Ulas,<sup>a</sup> Stefan-Sven Jester,<sup>‡a</sup> Patrick Weis,<sup>a</sup>  
 Artur Böttcher<sup>\*\*a</sup> and Manfred M. Kappes<sup>\*ab</sup>

Received 6th April 2010, Accepted 8th July 2010

DOI: 10.1039/c0cp00137f

This perspective focuses on the cage size dependent properties of novel solid fullerene nanofilms grown by soft-landing of mass-selected  $C_n^+$  (48, 50, 52, 54, 56, 58, 62, 64, 66 and 68) onto room temperature graphite surfaces under ultra-high vacuum conditions. Such non-isolated-pentagon-ring (non-IPR) fullerene materials are not accessible to standard fullerene preparation methods. The component molecular building blocks of non-IPR films were generated by electron impact induced ionization/fragmentation of sublimed IPR- $C_{70}(D_{5h})$  ( $\rightarrow C_n$  ( $n = 68, 66, 64, 62$ )) or IPR- $C_{60}(I_h)$  ( $\rightarrow C_n$  ( $n = 58, 56, 54, 52, 50$ )). Non-IPR fullerene films on graphite grow *via* formation of dendritic  $C_n$  aggregates, whereas deposition of IPR fullerenes under analogous conditions (*via* deposition of unfragmented  $C_{60}^+$  and  $C_{70}^+$ ) leads to compact islands. The latter are governed by weak van der Waals cage–cage interactions. In contrast, the former are stabilized by *covalent* intercage bonds as mediated by the non-IPR sites (primarily adjacent pentagon pairs, AP). A significant fraction of the deposited non-IPR  $C_n$  cages can be intactly (re)sublimed by heating. The corresponding mean desorption activation energies,  $E_{des}$ , increase from 2.1 eV for  $C_{68}$  up to 2.6 eV for  $C_{50}$ . The densities of states in the valence band regions (DOS), surface ionization potentials (sIP) and HOMO–LUMO gaps ( $\Delta$ ) of semiconducting non-IPR films were measured and found to vary strongly with cage size. Overall, the  $n$ -dependencies of these properties can be interpreted in terms of covalently interconnected oligomeric structures comprising the most stable (neutral)  $C_n$  isomers—as determined from density functional theory (DFT) calculations. Non-IPR fullerene films are the first known examples of elemental cluster materials in which the cluster building blocks are covalently but reversibly interconnected.

<sup>a</sup> Institut für Physikalische Chemie, and DFG-Center for Functional Nanostructures (CFN), Karlsruhe Institute of Technology (KIT), D-76128 Karlsruhe, Germany.

E-mail: artur.boettcher@chemie.uni-karlsruhe.de

<sup>b</sup> Institut für Nanotechnologie, Karlsruhe Institute of Technology (KIT), D-76128 Karlsruhe, Germany.

E-mail: manfred.kappes@chemie.uni-karlsruhe.de

<sup>†</sup> Present address: Fritz-Haber-Institut der Max-Planck-Gesellschaft, Berlin, Germany.

<sup>‡</sup> Present address: Institut für Organische Chemie, Universität Bonn, Bonn, Germany.

## 1. Introduction

Classical fullerenes are hollow-cage, even numbered, all-carbon clusters comprising pentagon and hexagon rings with each constituent carbon atom connected to three neighbours by strong covalent bonds. The structures of the well known classical fullerene cages,  $C_{60}(I_h)$  and  $C_{70}(D_{5h})$  are governed by the isolated pentagon rule, IPR,<sup>1,2</sup> which requires that all 12 constituting pentagons be surrounded by hexagonal rings and



Daniel Löffler



Seyithan Ulas



Stefan-Sven Jester



Patrick Weis

consequently separated from each other. Correspondingly, DFT-based calculations (presently the most accurate quantum chemical methods applied to this overall molecule class) predict significantly lower stability of strained non-IPR carbon cages in comparison to IPR cages of a given size.<sup>3</sup> It has furthermore been shown, that all classical fullerene cage structures possible for  $C_{20}$ – $C_{58}$  and  $C_{62}$ – $C_{68}$  violate the IPR rule.<sup>4</sup> For such  $C_n$  cage sizes, adjacent pentagon motifs (AP) are unavoidable. DFT calculations have also established that the energetic sequence of AP cage isomers of a given nuclearity typically follows the pentagon adjacency penalty rule (PAPR<sup>5</sup>), which relates the most stable carbon cages to the  $C_n$  structures with the minimum number of APs (except for  $C_{50}$ <sup>6</sup>).

Whereas non-IPR  $C_n$  hollow cages ( $n < 60$ ; 62–68) can be readily generated as stable molecules in gas phase, they remain practically uncharted in condensed phase.<sup>7,8</sup> In fact, during the last decade there have been numerous unsuccessful attempts to isolate non-IPR  $C_n$  cages generated in various fullerene soots.<sup>9,10</sup> In contrast, a number of *chemical derivatives* of non-IPR cages have recently been prepared in bulk scale and structurally characterized.<sup>11</sup> These structures typically indicate classical fullerene cages containing AP sites. Due to their increased pyramidal angles, such AP sites act as highly reactive centres<sup>12</sup> and the corresponding derivatives are often (exohedral) addition products in which C–C bonds shared between pairs of adjacent pentagons are saturated.<sup>13,14</sup> The addition products  $C_{36}H_6$ ,<sup>15</sup>  $C_{50}Cl_{10}$ ,<sup>16</sup>  $C_{54}Cl_8$ ,<sup>13</sup>  $C_{56}Cl_{10}$ ,<sup>16</sup>  $C_{64}H_4$ <sup>17</sup> and  $C_{66}X_4$  ( $X = H, F, Cl$ )<sup>18</sup> are cases in point. Bare, small non-IPR cages may also be stabilized by “endohedral derivatization”, *i.e.* by filling with one or more metal atoms to generate metallofullerenes (*e.g.*  $Sc_2@C_{66}$ ,<sup>19</sup> see also the review<sup>20</sup>). Usually, the endohedral metal atoms (ions) are coordinated to annelated-pentagon pairs thus facilitating electron transfer to the enclosing carbon cages which then become negatively charged.<sup>20,21</sup> So far there are only three well-documented cases of “non-classical” non-IPR fullerene derivatives:  $C_{58}F_{17}CF_3$ ,  $C_{58}F_{18}$ <sup>22</sup> and  $(4-Me-C_6H_4)_2C_{62}$ .<sup>23</sup> The fluorinated derivatives comprise cages with heptagon-rings (HP) and 13 pentagons each whereas the non-classical  $C_{62}$  cage exhibits a four-membered ring.

Small non-IPR  $C_n$  cages may be considered as carbon spheres functionalized by localized (AP or HP) reaction

centres. Thus, one might expect the growth of solid materials comprising such (bare) building blocks to involve self-stabilization by bond formation between reaction centres to yield polymeric chains and 3D structures,<sup>24</sup> as has been predicted by DFT calculations for solids consisting of  $C_{20}$ ,<sup>25</sup>  $C_{36}$ ,<sup>26,27</sup> and  $C_{50}$ .<sup>28</sup> In all of these calculations, quasi covalent inter-cage bonds between AP sites were indicated.

Such interlinked non-IPR fullerene films were first prepared by low-energy neutral cluster beam deposition onto a diamond target with a broad incident cluster size distribution centred between  $C_{20}$  and  $C_{32}$ .<sup>29–32</sup> We have more recently become interested in this issue and have applied mass selected ion beam soft landing (with incident kinetic energies,  $E_{kin} < 6$  eV) to generate multilayer films of various monodispersed non-IPR fullerenes on graphite targets.<sup>33</sup> In these experiments, the cation beams of non-IPR cages were generated by 40–100 eV electron-impact induced ionization and fragmentation of sublimed  $C_{60}(I_h)$ . This leads to ionization, sequential  $C_2$  loss and (following electrostatic collimation) to the corresponding generation of intense ion beams containing non-IPR cages with  $n = 50, 52, 54, 56$  and  $58$ .<sup>34</sup> The films generated by soft landing, exhibited thermal and electronic properties, which were clearly dependent on the size of the constituting non-IPR  $C_n$  cages.<sup>33,35</sup> In particular, we found that a good fraction of the incident non-IPR cages were intactly desorbable from the films by heating. However, significantly higher sublimation temperatures were required than necessary for the corresponding  $C_{60}(I_h)$  reference films. Preliminary AFM imaging revealed that the non-IPR  $C_n$  films grow according to the Volmer–Weber mechanism, reflecting aggregation of  $C_n$  cages as mediated by AP or HP reactive sites.

In the present study, we revisit thin films of non-IPR fullerene cages,<sup>35</sup> extend our previous work by performing further characterization and significantly expanding upon the size range of the building blocks. In particular, we have additionally deposited  $C_{68}$ ,  $C_{66}$ ,  $C_{64}$ , and  $C_{62}$  (generated by electron-impact induced ionization/heating of  $C_{70}(D_{5h})$ ) onto HOPG surfaces under soft-landing conditions. We compare the properties of the resulting thin films to those of smaller non-IPR fullerenes. Electronic properties were characterized by ultraviolet and X-ray photoelectron spectroscopies (UPS and XPS). Thermal stabilities were measured by thermal desorption spectroscopy, TDS. Topography of the resulting films was studied by means of atomic force microscopy, AFM. Our results demonstrate, how the electronic and thermodynamic properties of mono-dispersed  $C_n$  films (valence band, work function, surface ionization potential, HOMO–LUMO gap, intercage binding energy) depend on the nuclearity of the building blocks over a wide range of cage sizes ( $n = 48–70$ ).

## 2. Experimental methods

Non-IPR  $C_n$  films were grown on freshly cleaved pyrolytic graphite (HOPG, SPI Incorporated, SPI-II quality) by low energy ion beam deposition at a base pressure of better than  $5 \times 10^{-10}$  mbar. The  $C_n^+$  projectiles were generated by electron impact ionization/fragmentation of thermally sublimed IPR  $C_{60}$  or  $C_{70}$  emanating from a Knudsen cell.  $C_{60}(I_h)$  and  $C_{70}(D_{5h})$  were obtained as powders from Alfa



Artur Böttcher



Manfred M. Kappes

Aesar Company at 99.5% purity. Cations resulting from ionization were electrostatically collimated into an ion beam, which was passed through a 90° bender (to eliminate neutrals and anions) and a quadrupole mass selector (Extrel) before being directed onto a perpendicularly oriented highly oriented pyrolytic graphite target (HOPG). The mass selector resolution was chosen to allow baseline separation of neighboring  $C_{n-2}^+$  and  $C_{n+2}^+$  peaks from the selected  $C_n^+$  ( $\Delta m/m \approx 200$ ). Hence, the films grown were monodispersed without any measurable contaminants. The mean kinetic energy of  $C_n^+$  ions passing the quadrupole mass selector was set to *ca.* 34 eV in order to maximize ion flux. Soft-landing conditions were realized by applying an appropriate positive retarding potential to the HOPG target. This allowed reduction of the mean incident kinetic energy to  $\sim 6$  eV without significant loss of ion flux or broadening of the incident kinetic energy distribution (which had a width of less than 3 eV). All experiments described below were performed at constant mean kinetic energies of 6 eV using HOPG substrates held at room temperature,  $T_s = 300$  K.

The efficiency of electron impact induced fragmentation of  $C_{60}$  and  $C_{70}$  depends strongly on the electron kinetic energy,  $E_{el}$ .<sup>34</sup> When raising  $E_{el}$ , both the integral flux of all  $C_n^+$  as well as the degree of fragmentation increases. Consequently there is an optimal  $E_{el}$  value for each selected  $C_n^+$ , *e.g.*:  $E_{el} \approx 36$  eV for  $C_{68}$  and  $E_{el} \approx 85$  eV for  $C_{50}$ . All deposition experiments reported here were performed at such optimized  $E_{el}$  values (which also limit the extent of projectile vibrational excitation). Before deposition, the HOPG sample was flashed several times up to 1100 K under high vacuum in order to remove –OH and –C–H terminations of step edges. After cooling to room temperature and prior to deposition, the cleanliness of the substrate was established by taking UP and XP spectra.

Fullerene layer thickness was determined by measuring the neutralization current during deposition (picoamperemeter Keithley). The film thickness is given here in monolayer equivalents, MLE, whereby  $1\text{MLE} = 10^{14} \text{ cm}^{-2}$  (this corresponds roughly to the molecular packing density in crystalline solid  $C_{60}$ ). Attainable ion fluxes for film growth were  $n$  dependent, *e.g.*  $\sim 2$  nA for  $C_{68}^+$  and  $\sim 0.1$  nA for  $C_{50}^+$ . Consequently, the growth of a 6 MLE-thick film required  $\sim 1$  h and  $\sim 20$  h deposition times, for  $C_{68}$  and  $C_{50}$  respectively.

Thermal stability of  $C_n$  films was characterized by thermal desorption spectroscopy, TDS, using a second quadrupole mass spectrometer (Extrel; electron impact ionization) to monitor the flux of the  $C_n$  cages escaping from the solid film. All experiments were performed at the same heating rate of  $5 \text{ K s}^{-1}$ . The sample temperature during the TD scan was measured by means of a K-type thermocouple spot welded to the back side of the sample holder. The temperature in the central part of the sample surface was measured by means of a calibrated radiation pyrometer (Keller PZ20AF).

Valence-band electronic structure of deposited  $C_n$  films was studied by means of ultraviolet photoelectron spectroscopy, UPS (21.2 eV), using a hemispherical electron energy analyzer (ESI 125, Omicron, energy resolution of  $\sim 0.1$  eV) and a HeI-discharge lamp (Omicron). The relative alignment of the sample, lamp and electron analyzer was chosen to allow

for optimal detection of the normal component of the photoemission. The UP spectra mirror the density of states in the valence region, VB-DOS, and provide an easy method for measurement of the work function,  $\phi$ , and the surface ionization potential, sIP.<sup>35</sup> The XP spectra were taken by using a twin anode X-ray source (MgK $_{\alpha}$  line 1253.6 eV, DAR 400 Omicron) and the UPS hemispherical analyzer for electron energy determination.

Consistent with our foregoing work<sup>35</sup> all non-IPR fullerene films studied were found to be semiconducting as indicated by a significant gap between the highest occupied and the lowest unoccupied states. HOMO–LUMO gaps were determined by taking UP spectra after exposing the  $C_n$  films to a weak flux of Cs atoms (SAES Getters SpA,  $\sim 10^{14} \text{ Cs cm}^{-2} \text{ s}^{-1}$ ). This leads to measurable occupation of the LUMO-derived band, which manifests itself by an extra feature appearing in the UP spectra above the HOMO-derived band. The energy separation between the HOMO- and LUMO-derived bands is then a simple measure of the band gap.

The topography of deposited films was measured *ex situ* by atomic force microscopy, AFM, operating in the non-contact mode (AFM, Veeco Instruments CP-II). A  $5 \times 5$  micron scanner and NSC18 cantilevers with a nominal spring constant of  $4.5 \text{ N m}^{-1}$  were typically used. Systematic measurements of the lateral distribution of deposits revealed a rather flat macroscopic density profile with well recognizable edges—corresponding to the ion beam spot. The mean area covered by  $C_n$  cage deposits in a typical experiment was  $\sim 0.07 \text{ cm}^2$ .

### 3. Results and discussion

#### 3.1 AFM topography measurements: cage size dependence

The topography of films created by deposition of neutral  $C_{60}(I_h)$  or  $C_{70}(D_{5h})$  from effusive beams onto room temperature HOPG has been extensively studied by AFM.<sup>36</sup> Film growth is primarily determined by the relative strengths of van der Waals cage–cage interactions,  $E(C_n-C_n)$ , and slightly stronger cage–substrate interactions  $E(C_n-S)$ .<sup>37</sup> In the initial growth stages, some  $C_{60}$  ( $C_{70}$ ) cages are pinned at step edges and act as nucleation centres for cages migrating on flat terraces. The activation barrier for lateral diffusion on the graphite basal plane is very low ( $13 \text{ meV}$ )<sup>35</sup> and correspondingly the mobility of cages is high at room temperature.<sup>38</sup> At increasing coverages, this situation,  $E_{\text{diff}} \ll E(C_n-S) \approx E(C_n-C_n)$ , gives rise to the formation of 2D islands with smooth rims.<sup>39</sup> A diffusing  $C_{60}$  ( $C_{70}$ ) cage can only stick to an island rim if it finds a highly coordinating site. This stabilization criterion leads to lateral island growth, while at the same time the island peripheries become gradually smoother due to rim diffusion processes.

Fig. 1 (upper panel) shows two AFM images, which illustrate the formation of such compact 2D  $C_{60}(I_h)$  islands with smooth rims. Further deposition leads to the formation of small islands on top of the original 1 ML (= 2D) deposits—constituting the onset of second layer growth. These islands are however no longer smooth-rimmed because the underlying fullerene monolayer exhibits high corrugation and correspondingly higher activation energies for cage diffusion,



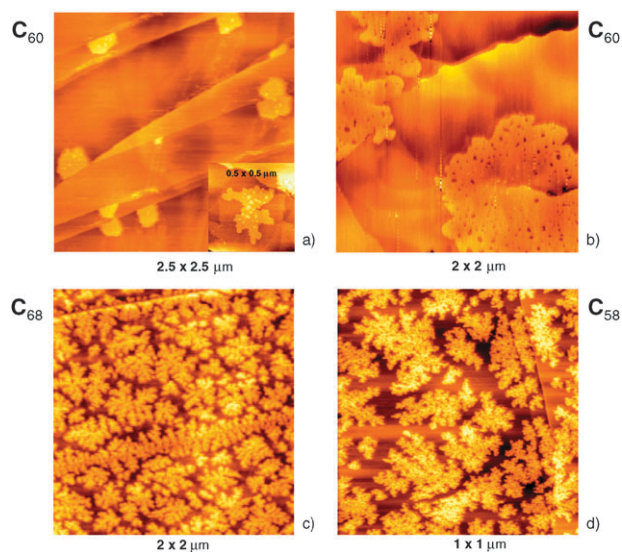


**Fig. 1** Upper panel shows two AFM images showing an HOPG surface after exposure to a low  $C_{60}^+$  dose at two different incident kinetic energies, 1 eV and 6 eV, (a) and (b) images, respectively ( $T_s = 300$  K). Only smooth rimmed, compact 2D  $C_{60}$  islands are observed. The inset in the left panel shows an example of second layer growth *via* formation of compact  $C_{60}$  aggregates on top of the first-layer island. The two deposition experiments also differ in terms of their  $C_{60}$  coverages (0.1 MLE and 0.5 MLE, left and right panel, respectively). Lower panel shows two AFM images taken after exposing HOPG surfaces to comparable doses of  $C_{68}^+$  and  $C_{58}^+$ , left (c) and right (d) panels (1.5 and 1 MLE, respectively;  $T_s = 300$  K,  $E_{kin} = 6$  eV). In all experiments with non-IPR  $C_n$  cages, we observed the formation of dendritic islands (see also ref. 43).

$E_{diff} \approx E(C_n-S)$  (various diffusion channels with  $E_{diff}$  ranging from 178 meV to 429 meV<sup>40</sup>). Correspondingly,  $E_{diff} \approx E(C_n-S) \approx E(C_n-C_n)$ , which leads to hindered lateral cage mobility and consequently dendritic on-top islands.<sup>40</sup> The inset in Fig. 1a shows an AFM image illustrating the shape difference between islands in the first and second layers. Note that the AFM images shown in the upper panel in Fig. 1 were obtained after depositing  $C_{60}^+$  ions onto HOPG under soft-landing conditions ( $T = 300$  K,  $E_{kin} = 1-6$  eV). They show surface topographies essentially identical to those found when depositing thermal energy (neutral)  $C_{60}$  cages.<sup>39</sup> Consequently, under our deposition conditions, impact-induced cage neutralization followed by cage thermalization does not appear to affect the island topography significantly—relative to films prepared by effusive beam deposition.

Before comparing the topography of IPR and non-IPR films it is useful to first consider DFT calculations performed for non-IPR fullerene cages interacting with a variety of different substrates ( $C_n$  ( $n = 28, \dots, 48, 60$ )/Si(001),<sup>41</sup>  $C_{20}$  oligomers,<sup>42</sup>  $C_{36}$  2D polymers,<sup>26,27</sup>  $C_{20}$ /Diamond<sup>25</sup>). These predict low energy covalently interlinked, three dimensional  $C_n$  cage architectures—with covalent bonds typically constituted by non-IPR sites (mostly 2AP-2AP—where 2AP indicates a cage surface site with two adjacent pentagons). Thus, the expectation is that non-IPR fullerene cage deposition should lead to porous/dendritic films exhibiting local arrangements of adjacent  $C_n$  cages, governed mainly

by their respective numbers of non-IPR sites as well as by the spatial distribution of these non-IPR sites over the cage surfaces.

Previously, we have focused on the surface topography of non-IPR  $C_{58}$  films deposited onto HOPG as studied by AFM.<sup>43</sup> The island shape was found to be strongly dependent on  $E_{kin}$  (within the range:  $1 \text{ eV} < E_{kin} < 40 \text{ eV}$ ) as well as on the surface temperature,  $T_s$  (varied from 200 K to 800 K) during deposition. Large dendritic 2D  $C_{58}$  islands are formed at low kinetic energies (and room temperature). These become smaller and more compact with increasing  $E_{kin}$ . The strongly dendritic islands also become more compact when depositing at elevated surface temperatures. These trends can be rationalized in terms of a mechanistic picture in which dissipation of incident kinetic energy must take place prior to cage attachment to (preformed) island peripheries. Two main loss mechanisms are involved: (1) inelastic conversion of the primary kinetic energy  $E_0$  of impacting cages into kinetic energy of parallel motion across terraces,  $E_{||}$  ( $E_{||} = \varepsilon E_0$  with the conversion coefficient  $\varepsilon$  depending on  $E_0$  according to  $\varepsilon(E_0 \text{ in eV}) = 0.3 \exp(-E_0/5.95) + 0.088$ ) and (2) decay of the  $E_{||}$  component, due to molecular friction acting on cages which move across the terraces with a velocity  $v$ ,  $E_{||}(t) = E_{||}(0)\exp(-\eta vt)$  ( $\eta = 8400 \text{ eVs m}^{-2}$ ).<sup>43</sup> One can envisage two qualitatively different sticking pathways, depending on the orientation of the  $C_n$  cages upon reaching an island: (i) all non-IPR sites of an incoming cage become involved in bonds to the island (or are shielded from further reaction) leaving only the “IPR” cage regions exposed, or (ii) one or more non-IPR reaction centres of the incoming cage remain exposed (and accessible for further bonding) after addition to a growing island. This distinction also applies to the dynamic case when a hyperthermal  $C_n$  cage strikes an island periphery terminated by cages which are oriented according to either (i) or (ii). One can then formally distinguish between four different local attachment types, A–A, A–B, B–A and B–B, differing considerably in interaction energies ( $E_{bind}$  ( $E(A-A) < E(A-B) = E(B-A) \ll E(B-B)$ ; with A and B referring to the IPR and non-IPR cage segments involved in the cage–cage interaction, respectively). In the A–A case the cage–cage interaction is van der Waals like ( $E(A-A) \approx 0.6 \text{ eV}$ <sup>44</sup>). In the second case, A–B or B–A, a significantly higher binding energy is expected. For the strongest B–B interactions, two adjacent non-IPR sites can form covalent bonds with the corresponding interaction energy being  $E_{bind} \approx 1.9 \text{ eV}$ .<sup>44</sup> Note that an on-terrace  $C_n$  cage moving with a lateral kinetic energy,  $E_{||}$ , can only stick at the periphery of a growing island if  $E_{||} < E_{bind}$  (neglecting barriers). Consequently, for hyperthermal kinetic energies, A–A and A–B pathways will have non-binding outcome unless dissipative processes have slowed the incoming cage to  $E_{||} < 1.9 \text{ eV}$ .

The  $C_{58}$  films grown by soft-landing at room temperature are metastable in a thermodynamic sense. We have previously inferred that A–A and A–B contacts can be converted into more stable B–B bonding states upon thermal annealing.<sup>43</sup> This activates the surface mobility of (previously) A–A and A–B interlinked cages. Upon encountering an exposed non-IPR reaction center, these can then form new quasi

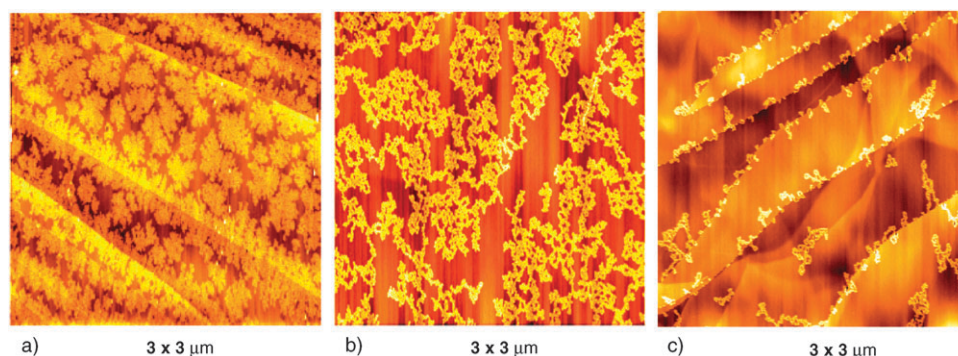


**Fig. 2** AFM images of HOPG surfaces: (a) after deposition of 1.5 MLE of  $C_{58}^+$  ions ( $E_{\text{kin}} = 6$  eV,  $T = 300$  K), (b) after annealing the  $C_{58}$  deposits to 550 K for 120 s, (c) after desorbing the majority of the deposits by linearly heating the sample up to 1100 K.

covalent bonds, (the B–B state). Correspondingly, tempering at elevated sample temperatures can *raise* the overall film thermodynamic stability due to an increase in the relative number of B–B interactions. Fig. 2 shows AFM images obtained for  $C_{58}$  deposits, which illustrate such a transformation as induced by 550 K annealing. Dendritic islands become converted into a polymeric network. At even higher annealing temperatures, desorption sets in and begins to compete with rearrangement. The AFM image taken after heating the surface to 1100 K shows that most of the deposited  $C_{58}$  material has been desorbed leaving a chain-like residue pinned at step edges. The molecular nature of this irreversibly bound material is presently the subject of further studies. It may conceivably derive from cage coalescence reactions which become significant within the desorption temperature range.<sup>45</sup>

AFM measurements were also performed on deposits of other non-IPR fullerene cage sizes:  $C_{50}$  and  $C_{68}$ . Under the same deposition conditions as used for  $C_{58}$  soft-landing, film growth was observed to proceed analogously. Three successive growth stages could be distinguished as coverage was increased: (1) pinning at HOPG step edges, (2) lateral growth of dendritic 2D islands on basal planes and (3) formation of the 3D “pyramidal” structures prior to complete wetting of the first monolayer (Vollmer–Weber growth mechanism).

The lower panel in Fig. 1 shows AFM images taken after deposition of comparable amounts of  $C_{58}$  and  $C_{68}$  onto HOPG ( $E_{\text{kin}} \approx 6$  eV,  $T_s = 300$  K). In contrast to the smooth rimmed  $C_{60}$  ( $I_h$ ) islands, all AFM images of the non-IPR films reveal dendritic island structures. Correspondingly, the lateral growth of an individual non-IPR fullerene island does not proceed homogeneously. Instead, discrete growth directions are preferred. These should ultimately be relatable to the relative alignment of non-IPR sites in individual cages (and the corresponding molecular structures). One might therefore expect significant differences between  $C_{50}$ ,  $C_{58}$  and  $C_{68}$  films, due to the fact that the respective cage structures may have very different numbers (and spatial distributions) of reactive sites. However, on the mesoscopic length scales resolvable with our present AFM setup, no striking differences were found among the island topographies studied. In future, we plan high-resolution STM studies to further examine this issue.

## 3.2 Thermal stability

**3.2.1 Non-IPR fullerene films:  $C_{58}$  versus  $C_{68}$ .** Fig. 3a shows a series of thermal desorption spectra obtained by monitoring the flux of  $C_{68}$  molecules escaping from linearly heated HOPG surfaces covered by  $C_{68}$  films of various thicknesses. The corresponding measurement for a film of the parent IPR  $C_{70}(D_{5h})$  is also shown (grey curve). Note, that the maxima of the broad  $C_{68}$ -TD spectra are located at higher temperatures than for  $C_{70}$ -TD, indicating considerably higher thermal stability. At comparable coverages,  $C_{68}$ -TD bands are at least twice as broad as those of  $C_{70}$  ( $\delta w(C_{68}) \approx 115$  K and  $\delta w(C_{70}) \approx 55$  K). At very low coverages, the  $C_{68}$ -TD desorption maximum is centered at  $\sim 760$  K. The desorption maximum shifts towards higher temperatures at higher coverages—levelling off at 815 K for  $>1$  ML thick films. According to a simple Redhead analysis, the activation energy for desorption is proportional to the temperature at which the maximum desorption rate is observed,  $T_m$ .<sup>46</sup> Thus, the significant upshift with increasing coverage indicates a corresponding increase in the binding energy of  $C_{68}$  cages. For the thickest films, a  $C_{68}$  desorption activation energy of 2.1 eV per cage can be derived from the measurements.

As previously mentioned, the initial  $C_{68}$  film growth stage is characterized by step edge decoration (and empty basal planes). Thus, the peak in the  $C_{68}$ -TD spectrum observed for low coverages  $\leq 0.5$  MLE ( $T_m \approx 760$  K) can be assigned to cages pinned by reactive sites terminating the step edges,  $-C-C_n$ . The activation energy for desorption of  $C_{68}$  cages from such sites appears to be slightly lower than for desorption from 3D islands in thick films.

Fig. 3b shows corresponding  $C_{58}$ -TD spectra as a function of coverage. Compared to  $C_{68}$  they show a higher desorption maximum centred at 860 K (for thick films). In contrast, comparably thick  $C_{60}$  films show a narrower desorption maximum (grey curve) located at much lower temperatures—around 580 K. Mean desorption activation energies derived from a Redhead analysis were 2.35 eV and 1.63 eV for  $C_{58}$  and  $C_{60}$ , respectively. The most striking difference between  $C_{68}$ - and  $C_{58}$ -TD spectra concerns the width of desorption bands:  $C_{58}$  features are significantly *broader* ( $\delta w(C_{58}) \approx 180$  K *versus*  $\delta w(C_{68}) \approx 115$  K). Nevertheless, compared to the much narrower parent IPR fullerene desorption features

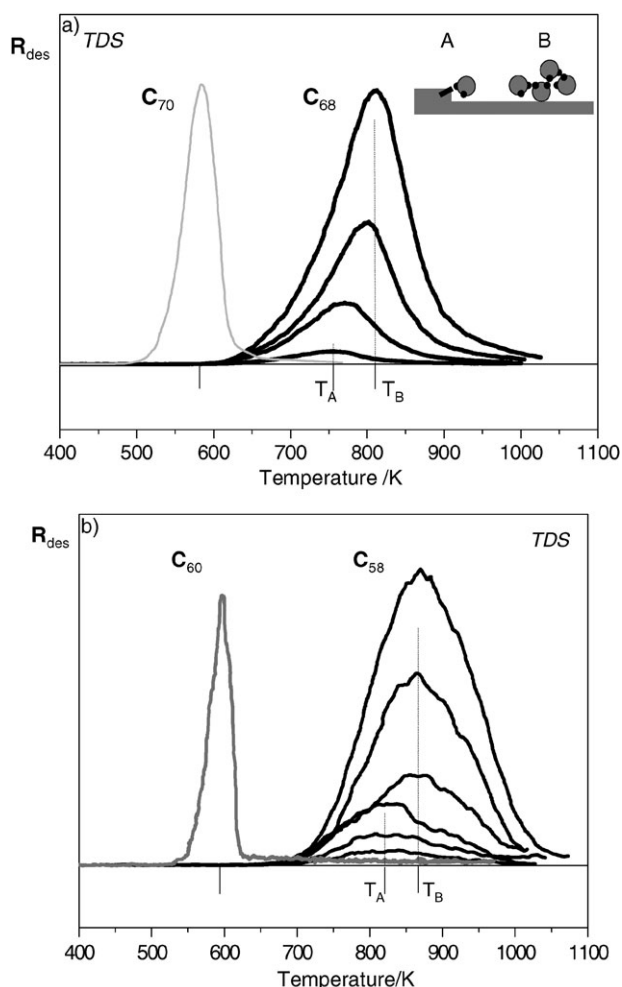


**Fig. 3** (a)  $C_{68}$ -TD spectra obtained for four different  $C_{68}$  coverages (0.4, 1, 2.5 and 5 MLE;  $E_{\text{kin}} = 6$  eV,  $T = 300$  K). The grey curve shows a  $C_{70}$ -TD spectrum taken for a  $\sim 2$  ML thick  $C_{70}$  film. Note the considerably higher thermal stability of the non-IPR  $C_{68}$  film. The inset schematically shows the oligomeric structures responsible for the observed temperature shift,  $T_A \rightarrow T_B$ . All spectra were taken at the same constant heating rate of  $5 \text{ K s}^{-1}$ . (b)  $C_{58}$ -TD spectra taken for several nominal coverages (0.5, 1.1, 1.7, 4.4, 8.5 and 16 MLE, respectively; deposition conditions as in the previous figure). For comparison the  $C_{60}$ -TD spectrum obtained for a 1.6 MLE thick film is also shown (grey curve). Note the pronounced difference in the thermal stability of the IPR and non-IPR films. All spectra were taken at the same constant heating rate of  $5 \text{ K s}^{-1}$ .

( $\delta w(C_{60}) \approx 35 \text{ K}$  and  $\delta w(C_{70}) \approx 55 \text{ K}$ ),  $C_{58}$  and  $C_{68}$  TD bands are qualitatively similar.

As noted above, theoretical predictions of stable networks of non-IPR cages,  $C_{20}$ ,  $C_{36}$  and  $C_{50}$  have demonstrated enhanced cohesion due to quasi-covalent intercage links as e.g. mediated by adjacent pentagon (AP) sites.<sup>47</sup> Similarly, we interpret the enhanced thermal stabilities of non-IPR  $C_{58}$  and  $C_{68}$  films as reflecting covalent  $-C_n-C_n-$  oligomer formation. The differences in sublimation energies and widths of desorption bands ( $E_{\text{des}}(C_{68}) < E_{\text{des}}(C_{58})$  and  $\delta w(C_{68}) < \delta w(C_{58})$ ) must then reflect differences between the respective non-IPR cage molecular structures and associated differences between the strengths of their intercage bonding. Following the

terminology of the previous section, we equate the average sublimation energy with the total binding energy of a given cage (to all surrounding cages ( $E_{\text{subl}} = kE(A-A) + lE(A-B) + mE(B-B)$ , where  $k$ ,  $l$ ,  $m$  are the mean numbers of type A-A, A-B and B-B bonds in a typical subliming cage, respectively)). For equivalent bonds,  $E_{\text{des}}$  scales with the mean coordination number of a cage,  $k + l + m$ . However,  $E(B-B) \gg E(B-A) > E(A-A)$  and consequently,  $E_{\text{des}} \approx mE(B-B)$ , where  $m$  corresponds to the mean number of non-IPR sites per cage. We therefore rationalize the higher thermal stability of the smaller non-IPR fullerene film,  $E_{\text{des}}(C_{68}) < E_{\text{des}}(C_{58})$ , as indicating that  $m(C_{68}) < m(C_{58})$  (see also note 48).

### 3.2.2 Film compositions: DFT predictions of cage isomers.

We presently have no unequivocal experimental data on the molecular structures (or isomer distributions) of deposited cages and therefore proceed to a discussion based on structure predictions from DFT theory. Given the comparatively long experimental timescale between ionization and deposition ( $\sim 100 \mu\text{s}$ ), it is plausible, that in each case the lowest (free) energy cage isomers of the corresponding *cations* are soft-landed. However, the size-dependent details of energy dissipation and cage rearrangements following electron impact are unclear. Furthermore, (additional) cage rearrangement may be associated with surface neutralization and impact heating. Consequently, we must discuss the structures of deposited cages in terms of predictions for the lowest energy isomeric forms of both singly positively and neutral cages of a given nuclearity. DFT calculations find that the lowest energy cage isomers for both charge states are *conventional fullerene cages* with one exception ( $n = 62$  which is predicted to have a lowest energy HP-containing isomer). Furthermore, these DFT calculations<sup>49,50</sup> (see Table 1) suggest that in the size range of interest here, the lowest energy singly charged cations and neutrals *have the same cage structures*—except for  $n = 50$ , 66 and 68. As mentioned previously, the most stable  $C_n^{(+)}$  cages differ by the number of reactive C-C bonds  $m$  shared between two adjacent pentagons. *Interestingly, the most stable  $C_n$  and  $C_n^+$  pairs always exhibit the same  $m$  values* (except for  $C_{50}$ , see Table 1).

$C_{68}[C_2: 0112]$  and  $C_{58}[C_{3v}: 0001]$  are calculated to have  $m = 2$  and  $m = 3$  reactive bonds, respectively.<sup>51,52</sup> Thus, if we assume that the overall desorption activation energy scales linearly with the number of such sites, the inequality  $E_{\text{des}}(C_{68}) \approx 2E(B-B) < 3E(B-B) \approx E_{\text{des}}(C_{58})$  holds. (note 53). The broad desorption curves obtained for the two non-IPR fullerene films (Fig. 3) can then be rationalized to first order as the result of a broad distributions of differently bonded cages (which would correspondingly escape at different temperatures). Furthermore, the difference,  $\delta w(C_{68}) < \delta w(C_{58})$ , may be explained by the fact that a  $C_{58}[C_{3v}: 0112]$  cage can be stabilized by forming one, two or three 2AP-2AP bonds with the surrounding cages whereas a  $C_{68}[C_2: 0112]$  cage can only be one- or two-fold coordinated (as  $m = 2$ ).

The thermal desorption behaviour discussed so far for  $C_{68}$  and  $C_{58}$  films was found to be qualitatively the same for all other non-IPR fullerene films studied (from  $C_{50}$  to  $C_{68}$ ). Fig. 4 illustrates this generality. Shown are TD spectra for



**Table 1** Structural parameters of the most stable neutral and singly positively charged fullerenes,  $C_n$  and  $C_n^+$ , according to DFT calculations<sup>46,64a</sup>

Cage isomer		Symmetry		Structural motifs		$m$	
$C_n$		$C_n^{(0)}$	$C_n^{(+)}$	$C_n^{(0)}$	$C_n^{(+)}$	$C_n^{(0)}$	$C_n^{(+)}$
$C_{70}$	(6000)	$D_{5h}$		IPR		0	<b>0</b>
<b><math>C_{68}</math></b>	(3981)	$C_2$	<b>(<math>C_2</math>)</b>	2-2AP	<b>(2-2AP)</b>	2	<b>(2)</b>
<b><math>C_{66}</math></b>	(1789)	$C_s$	<b>(<math>C_{2v}</math>)</b>	1-C3AP	<b>(2-2AP)</b>	2	<b>(2)</b>
$C_{64}$	(1998)	$D_2$		2-2AP		2	<b>2</b>
$C_{62}$	(1994)	$C_2$		1-C4AP + 1 HP		3 + HP	<b>3</b>
$C_{60}$	(1812)	$I_h$		IPR		0	<b>0</b>
$C_{58}$	(1205)	$C_{3v}$		3-2AP		3	<b>3</b>
$C_{56}$	(916)	$D_2$		4-2AP		4	<b>4</b>
$C_{54}$	(540)	$C_{2v}$		2-C3AP		4	<b>4</b>
$C_{52}$	(422)	$C_2$		2-C3AP + 1-2AP		5	<b>5</b>
<b><math>C_{50}</math></b>	(270)	$D_3$	<b>(<math>D_{5h}</math>)</b>	6-2AP	<b>(5-2AP)</b>	6	<b>(5)</b>
	(271)	$D_{5h}$		5-2AP		5	<b>5</b>

<sup>a</sup> The cage isomers are labelled according to the Fowler and Manolopoulos scheme.<sup>69</sup> In addition to molecular symmetries, we have also tabulated the corresponding structural motifs (C4AP, C3AP, 2AP and HP refer to chain of four adjacent pentagons, chain of three adjacent pentagons, two adjacent pentagons and heptagon ring, respectively). Also listed are the number of common C–C bonds shared between adjacent pentagons,  $m$ . Where the structures of neutral and cationic  $C_n$  cages of a given  $n$  differ, the entries for the cationic cages are given in italic parentheses (and bold face). This is only the case for:  $C_{50}$ ,  $C_{66}$  and  $C_{68}$ . Excepting  $n = 50$ , the same  $m$  is found for all  $C_n/C_n^+$ . Whereas the most stable form of  $C_{50}$  exhibits six 2AP sites (and therefore six common bonds) the corresponding cation  $C_{50}^+$  has only five. Tabulated  $m(n)$  values are the averages of the  $m$  values for  $C_n^{(0)}$  and  $C_n^{(+)}$ . <sup>b</sup> We included two  $C_{50}$  isomers ( $D_3$  and  $D_{5h}$ ) as representing the common lowest isomer because according to DFT calculations they exhibit nearly the same values of the total energy.

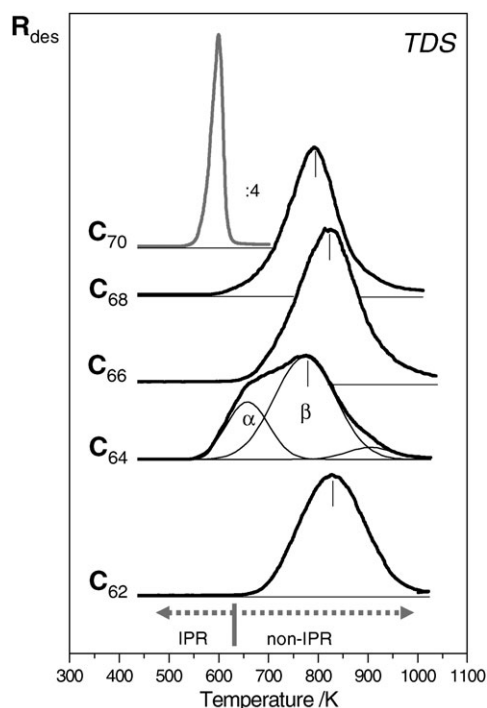


**Fig. 4** Thermal desorption spectra obtained for thick films of non-IPR fullerenes obtained by soft-landing the corresponding [ $C_{70}$ ]-derived fragment ions:  $C_{68}$ ,  $C_{66}$ ,  $C_{64}$  and  $C_{62}$  ( $T_s = 300$  K and  $E_{kin} = 6$  eV, 20 MLE thick films). For comparison the TD spectrum of the parent  $C_{70}$  cages is also shown (grey line curve). All spectra were taken at the same constant heating rate of  $5$  K  $s^{-1}$ .

~20 MLE-thick monodispersed  $C_n$  films ( $C_{68}$ ,  $C_{66}$ ,  $C_{64}$  and  $C_{62}$ ; deposited at  $T_s = 300$  K and  $E_{kin} \approx 6$  eV). In comparison to a  $C_{70}(D_{5h})$  film of comparable thickness, all non-IPR films exhibit much higher sublimation temperatures. Corresponding

$T_m$  values lie between 775 K and 825 K and exhibit a clear cage-size dependence. Again all TD spectra manifest considerably broader desorption bands than found for  $C_{70}$ . Interestingly,  $C_{64}$ -TD spectra are approximately twice as wide as the others and clearly consist of at least two Gauss-like components indicating the presence of two distinguishable isomers.<sup>54</sup>

We have previously reported analogous TD measurements<sup>33,35</sup> for films of  $C_n$  ( $n = 50, 52, 54, 56$  and  $58$ ) resulting from fragmentation of  $C_{60}(I_h)$  cages ( $T_s = 300$  K,  $E_{kin} \approx 6$  eV). In analogy to the  $C_{62}$ – $C_{68}$  series, the thermal properties of  $C_{50}$ – $C_{58}$  films were also strongly dependent on cage size, with  $T_m$  values ranging from 815 K for  $C_{58}$  up to 950 K for  $C_{50}$ . Similarly, the smaller the cage, the wider the TD spectra—ranging up to  $\delta w(C_{50}) \sim 210$  K.

Fig. 5 summarizes the size dependencies of the mean desorption activation energies for all TD measurements. In general, the smaller the non-IPR cages, the higher the film desorption activation energies,  $E_{des}(C_n)$ . These ranged from 2.1 eV for  $C_{68}$  to 2.6 eV for  $C_{50}$  films—depending rather smoothly on  $n$ . The only significant departures from this trend were found for the parent  $C_{60}$  and  $C_{70}$  IPR fullerene films (1.55 eV and 1.65 eV, respectively, in good agreement with published data<sup>55</sup>). For the non-IPR cages, we note that the  $m$  values corresponding to the lowest energy, DFT-based, cage isomers also increase with decreasing size—from 2 for  $C_{68}$  up to 5 and 6 for the two lowest  $C_{50}$  isomers. Consequently, the general trend apparent in Fig. 5 can be qualitatively rationalized in terms of the mean numbers  $m$  of pentagon-adjacencies on the respective cages and by the associated mean coordination numbers (see Table 1). Assuming, that these are in fact the deposited molecular structures, one can calculate the mean dissociation energy per –2AP–2AP– connection,  $\varepsilon(n) = E_{des}(C_n)/m$ .<sup>56</sup> This results in:  $\varepsilon(n) = -1.47 + 0.038n$ . Note, that the dissociation energies of 2AP–2AP connections as derived from DFT calculations for isolated dimers (2.61 eV



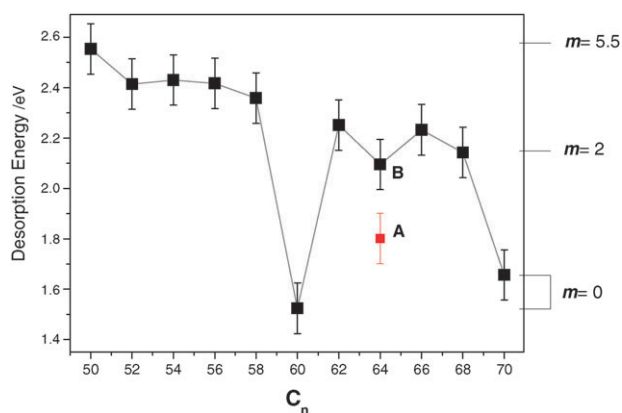


**Fig. 5** Desorption activation energies,  $E_{\text{des}}$ , versus the number of carbon atoms per cage,  $n$ . The data were gained in the sublimation regime, *i.e.* for film thickness  $\sim 20$  MLE. Note that  $E_{\text{des}}$  values scale with the average number of non-IPR sites per cage  $m$  (= AP sites)—when assuming that the films consist of most stable  $C_n$  isomers as determined by DFT calculations (the corresponding  $m$  values are indicated at the right margin as well as in Table 1). For  $C_{64}$  films two distinguishable desorption states were found—marked as A and B. In this context, see also ref. 66 which reports a desorption activation energy of  $\sim 1.9$  eV for  $C_{60}(C_{2v})$  having  $m = 2$ .

for a  $C_{50} = C_{50}$  connection, and 1.93 eV for  $C_{58} = C_{58}^{44}$ ) are considerably higher than the  $\varepsilon(n)$  values determined from experiment. Moreover,  $\varepsilon(n)$  values were observed to *increase* with cage size—in contrast to computed dissociation energies, which show the opposite trend. We conclude, that the actual mean number of 2AP–2AP inter-cage interactions present in non-IPR  $C_n$  solids,  $m^*$ , must be significantly smaller than  $m$  because of steric constraints (dependent on cage size and spatial distribution of AP sites) which can hinder the formation of intercage connections. Additionally (and particularly on the highly corrugated surface of a multi-ML film), A–A and A–B states might present a kinetic hindrance for formation of B–B links because of the random nature of the soft-landing and surface transport events.

As indicated by Fig. 1 and 2 as well as by our previous work,<sup>35,43</sup> in the low-coverage range the desorption yield as well as the temperature of maximum desorption rate depend significantly on substrate topography (atomic defects, step edges, grain boundaries, *etc.*). The above discussion of  $C_n$  desorption/sublimation activation energies is based on data obtained in the *sublimation* regime (thick films) in which the positions of TD maxima are essentially independent of film thickness. Note, however, that sublimation of individual non-IPR cages at elevated sample temperatures competes with irreversible coalescence/fusion to yield stable non-desorbable conducting networks. The latter reaction is expected to be facilitated by a precursor arrangement of  $C_n$  cages with highest possible  $m^*$ -values whereas sublimation preferentially occurs from low  $m^*$ -value areas. Details will be discussed in a separate paper (Ulas *et al.*<sup>57</sup>).

### 3.3 Electronic structure

**3.3.1 HOMO-derived valence bands.** The electronic structure of non-IPR  $C_n$  films was characterized using UPS

(He 21.2 eV) and XPS ( $\text{MgK}\alpha$  1253.6 eV) with particular emphasis on the valence band (VB) regions and their cage size dependence.

We first focus on  $C_{68}$  and  $C_{58}$  films and compare their VB structure to those of IPR  $C_{70}$  and  $C_{60}$  films (Fig. 6). The latter spectra are both in good agreement with the literature.<sup>58</sup> Whereas the HOMO-derived band of  $C_{70}$  films exhibits five distinguishable components, the  $C_{68}$ -HOMO-derived band comprises a broad doublet significantly shifted towards the Fermi level ( $\Delta E \approx 0.3$  eV) (Fig. 6a). By contrast, a comparison of  $C_{60}$  and  $C_{58}$  films reveals qualitatively different behaviour. Whereas the  $C_{60}$ -HOMO-derived band consists of a doublet with two sharp nearly Gaussian components, the HOMO-band of the  $C_{58}$  film exhibits three distinguishable components shifted towards  $E_F$  by  $\sim 0.5$  eV (Fig. 6b). For both non-IPR films, the observed changes relative to films of the respective

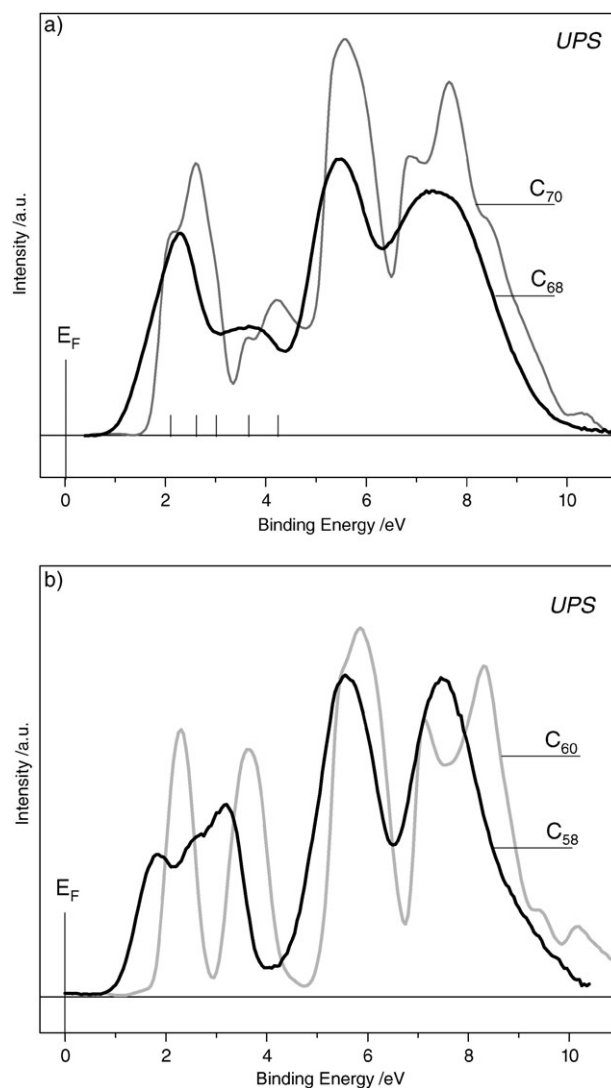


**Fig. 6** Densities of states in the valence bands, DOS-VB, as monitored by ultraviolet photoelectron spectroscopy, UPS ( $h\nu = 21.2$  eV) for 8 MLE  $C_{68}$  and  $C_{58}$  films, panels a and b, respectively. For comparison, the DOS-VB bands obtained for comparably thick films of the parent  $C_{70}$  and  $C_{60}$  IPR cages are also shown (grey curves) in the upper and lower panels, respectively.

precursor IPR cages are likely due to the 2AP structural motifs of the building blocks as well their covalent interconnections ( $m = 2$  and 3 for ground state  $C_{68}$  and  $C_{58}$  isomers, respectively). As we have previously shown, DFT-based calculations of the densities of electronic states for short  $C_{58}$  oligomers interlinked by  $-AP-AP-$  bonds, recover the triplet HOMO-DOS structure shown in Fig. 6b. Correspondingly, we have tentatively suggested that this triplet—in particular its central component—may be a general marker for AP sites and inter-cage bonds in non-IPR fullerene films. Support for this view was obtained by analogous features seen in UPS spectra of  $C_{56}$ ,  $C_{54}$ ,  $C_{52}$  and  $C_{50}$  films. However, the  $C_{68}$ -HOMO-derived broadened doublet band shown in Fig. 6b is in

contradiction with this simple 2AP “electronic fingerprint” view. Fig. 7 illustrates this point further. It shows expanded scale segments of the UP spectra obtained for comparably thick  $C_n$  films, from  $C_{70}$  to  $C_{48}$ .<sup>59</sup> Superimposed on these HOMO-derived band regions are Gaussian fits to the data. Whereas the HOMO-derived bands of the  $[C_{60}]$  fragment family could be well fit with only *three* Gaussian components (labelled  $\nu$ ,  $\eta$  and  $\mu$ ), the  $[C_{70}]$ -derived fragment  $C_n$  cages required at least *four* Gaussian components ( $\alpha$ ,  $\beta$ ,  $\gamma$  and  $\delta$ ), in order to obtain comparably good fits (Fig. 7). Apparently, the electronic signature of interdependent/interconnected AP-AP sites depends strongly on the size and symmetry of the component cages. The distinct trends in the HOMO( $n$ )

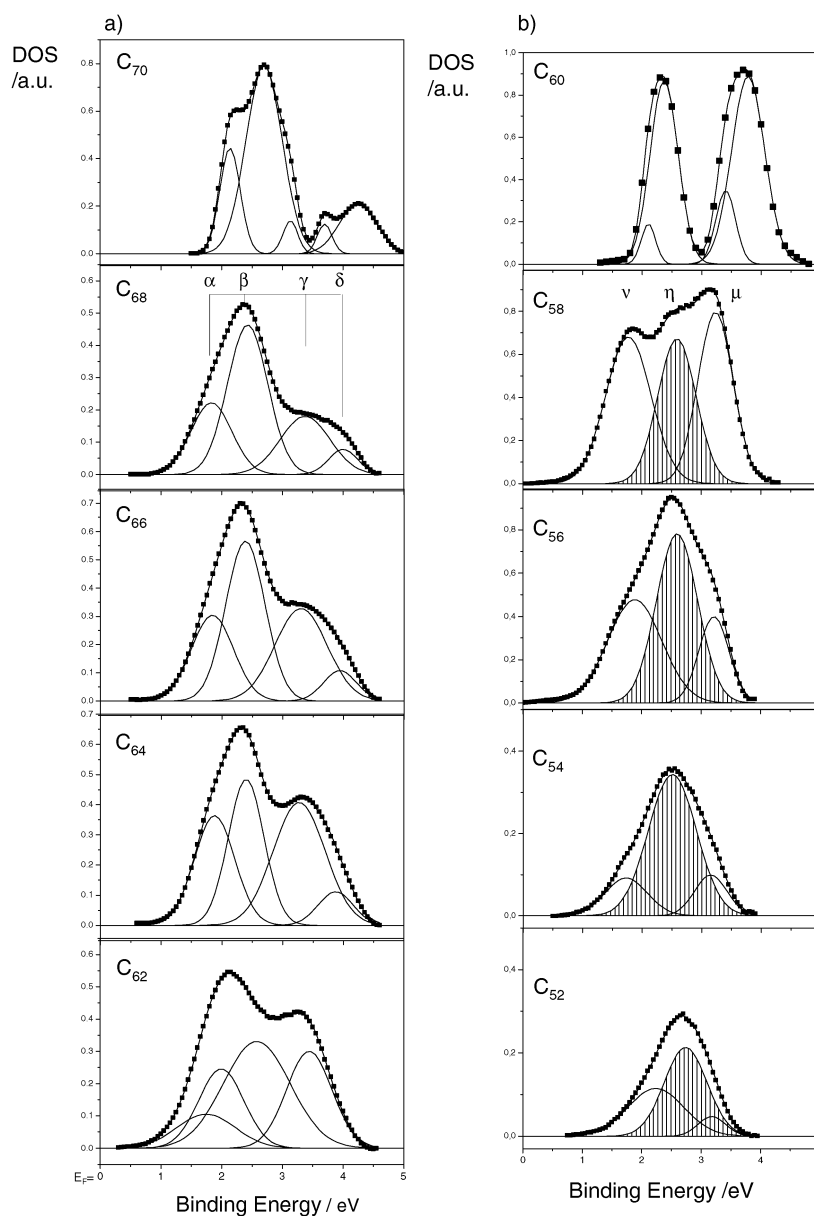


**Fig. 7** DOS-HOMO-derived bands *versus* cage size for 6–12 MLE thick films of non-IPR fullerenes generated as fragment ions by electron impact ionization of  $C_{70}$  and  $C_{60}$ , panels *a* and *b*, respectively. The DOS-HOMO-derived bands in the  $[C_{70}]$  group have been best-fitted with four Gaussian components,  $\alpha$ ,  $\beta$ ,  $\gamma$  and  $\delta$ , centred at 1.8, 2.35, 3.4 and 4 eV, respectively. In contrast, the DOS-HOMO-derived bands of the  $[C_{60}]$  family were satisfactorily fitted using only three Gaussian profiles,  $\nu$ ,  $\eta$ , and  $\mu$  peaked at 1.7, 2.55 and 3.35 eV, respectively. In each case we show the best fits for the minimum number of components.

dependencies found here for members of the two families [ $C_{60}$ ] and [ $C_{70}$ ] implies that there is no common electronic signature of AP–AP links for all cages. Instead the HOMO-DOS seems to mirror merely the origin of the  $C_n$  cage ([ $C_{60}$ ] or [ $C_{70}$ ] family). In future, it will be of interest to systematically compare experimental spectra with DOS calculations of model oligomers—taking into account DFT calculations of the most stable  $C_n$  isomers for each  $n$  (and/or experimental data on actual molecular structures).<sup>47–52</sup> This will help to understand the dependence of the DOS: (i) on the respective 2AP local geometries (e.g. pentagon face sharing C–C, bond lengths<sup>47,51,60</sup> and associated pyramidalization angles<sup>13</sup>) as well as (ii) on the lateral distributions of AP sites over the cage “surfaces”.

**3.3.2 Ionization potentials.** The size dependence of the ionization energies of isolated  $C_n$  cages can be modelled in terms of a hollow metallic sphere with homogeneous charge distribution<sup>61</sup> leading to the relationship:  $IP = IP_\infty + e^2/2R$ , where  $R$  is the cage radius and  $IP_\infty$  is the ionization potential for  $R \rightarrow \infty$ . Corresponding measurements on gas-phase  $C_n$  cages confirm the main trend but also resolve significant cage-size dependent deviations. It is interesting to consider to what extent matrix interactions and in particular the formation of oligomeric chains in non-IPR solid films modifies the “surface ionization potentials”,  $sIP(R)$ , of these cages relative to the IP values of individual cages isolated in gas-phase. Surface ionisation potentials can be determined from film work functions,  $\phi$ , and the energies of the topmost occupied states,  $E_B(\text{HOMO})$ , according to  $sIP = E_B(\text{HOMO}) + \phi$ . We obtained  $\phi$  values from the UP spectral widths,  $W$ , according to  $\phi = h\nu - W$ . This in turn required identification/assignment of the vacuum and Fermi levels in the spectra, which together constrain  $W$ . In our UP spectra, the HOPG substrate defines the Fermi level. For all thick  $C_n$  films, we measured similar values ranging from 4.7 eV up to 4.8 eV. Thus, within experimental error of  $\pm 0.06$  eV, non-IPR films have a common work-function of 4.75 eV. To within similar accuracies, we determined the work functions of  $C_{60}$  and  $C_{70}$  films to be 4.6 eV and 4.7 eV, respectively.  $E_B(\text{HOMO})$  values were obtained by fitting HOMO-derived-bands with Gaussian functions and assigning  $E_B(\text{HOMO})$  as the energy of the peak maximum corresponding to lowest binding energy Gaussian component. Fig. 8 illustrates the resulting  $sIP(n)$  values for  $48 \leq n \leq 70$  (black squares).<sup>62</sup> For comparison, we also show IP values as obtained from DFT calculations for the lowest energy  $C_n$  cage isomers as found at the B3LYP/6-31 G level of theory<sup>44,63,64</sup> (open circles) as well as the experimental data obtained for gas phase cages<sup>65</sup> (grey circles). There is an unexpectedly clear correlation between experimental  $sIP(n)$  and DFT-IP( $n$ ) values. We note that our procedure for determining  $sIP(n)$  as applied to a mixture, would yield a value corresponding to its lowest  $sIP$  component. This could conceivably correspond to the selective ionization of weakly A–A bound non-IPR cages embedded within a more strongly (B–B) covalently bound oligomeric matrix.

**3.3.3 HOMO–LUMO gaps.** The gaps between the HOMO- and LUMO-derived bands of non-IPR  $C_n$  films can

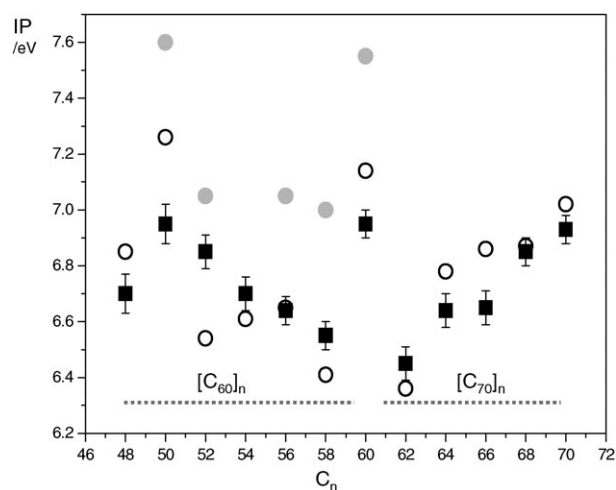


**Fig. 8** Surface ionization potentials,  $sIP$ , as measured for 6–12 MLE fullerene films as a function of cage size, black squares. Corresponding, DFT-derived IP predictions for the most stable isomers are presented by open circles.<sup>64</sup> The IP values measured for gas-phase  $C_n$  ( $n < 60$ ) cages are marked by grey full circles<sup>65</sup> (see also Table 2 which lists IP values calculated for the most stable  $C_n$  isomers).

be determined by UPS if measurable occupation of LUMO-derived bands is provided for by doping with electropositive atoms. In such doping, two requirements have to be fulfilled: (1) the ionisation energy of the dopant atoms should be lower than the binding energy of the LUMO-derived band, ( $E_i < E(\text{LUMO})$  with respect to the vacuum level) and (2) the relative concentration of dopant atoms should be as low as possible in order to avoid the formation of stoichiometric fulleride phases stabilized by periodically arranged cations (resulting from the associated electron transfer process,  $C_n + A \rightarrow C_n^- + A^+$ ). Consequently, we have deposited small and comparable amounts of Cs atoms ( $\sim 2 \times 10^{15} \text{ cm}^{-2}$ ) onto thick  $C_n$  films and have then measured the complete occupied valence band regions by UPS. Fig. 9 illustrates two representative examples of the modifications observed upon Cs-doping  $C_{70}$  and  $C_{68}$ , panels (a) and (b), respectively. In order to interpret these spectra, the energetic positions of the newly occupied LUMO-derived bands were determined by fitting the valence band regions with (the minimum necessary number of) Gaussian components. The striped Gaussian profiles shown in Fig. 9 indicate the corresponding LUMO-derived bands. We take the energy difference between the peak maximum of the highest HOMO component and that of the new LUMO-band as a simple measure of the actual band gap,  $\Delta$ . Fig. 10 summarizes the  $\Delta$  data obtained for all  $C_n$  films ( $48 \leq n \leq 70$ ).

For  $C_{70}$  films we measured gap values ranging between 2.05 and 2.15 eV—somewhat higher than previously found for  $C_{60}$  films ( $\Delta \approx 1.95 \text{ eV}$ <sup>66</sup>). In general, non-IPR films exhibited lower  $\Delta$  values than did films of their IPR  $C_{60}$  and  $C_{70}$  precursors. They ranged from 0.8 eV to 1.8 eV. [ $C_{70}$ ]-fragment derived non-IPR films generally have significantly higher  $\Delta$  values than do films of (smaller) [ $C_{60}$ ] derived cages (including  $C_{48}$ ). As previously pointed out,  $C_{50}$  represents an exception in this regard in that its  $\Delta$  value (1.7 eV), is comparable to those of  $C_{60}$  and  $C_{70}$  films. This



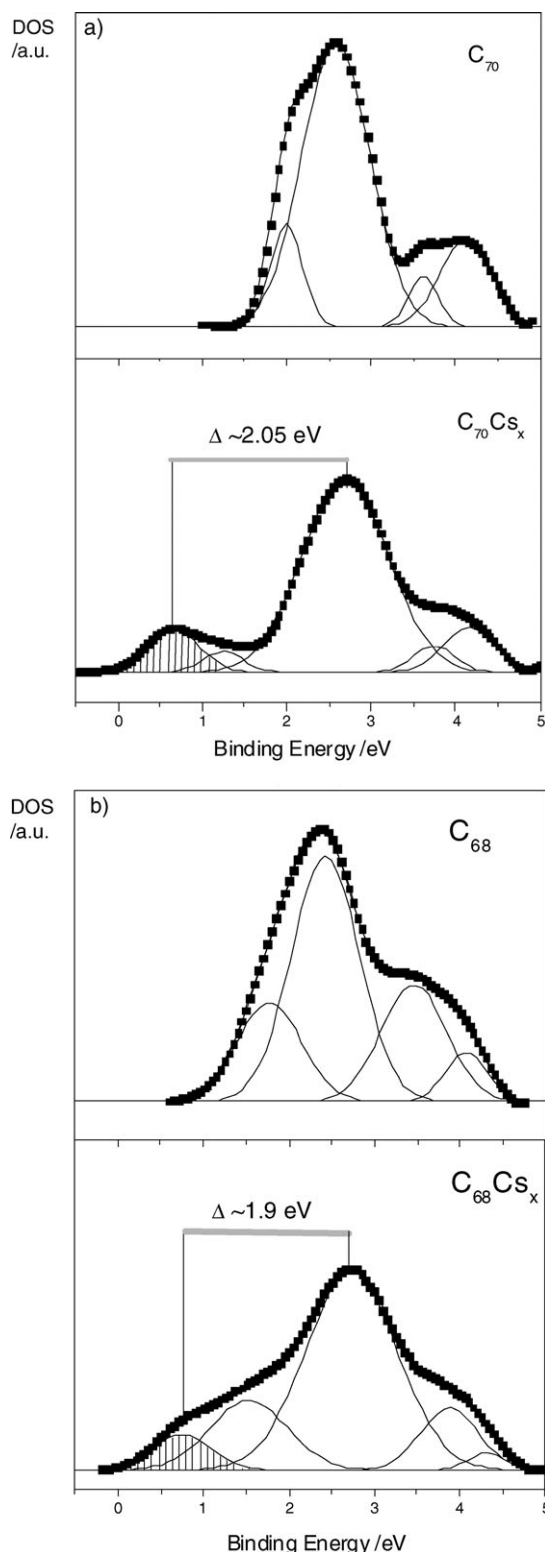


**Fig. 9** UPS derived densities of states in the valence band regions, DOS-VB, showing the effect of Cs doping of 8 MLE-thick films,  $C_{70}$  and  $C_{68}$  films, (a) and (b), respectively. Upper and lower panels correspond to pristine and Cs-doped phases, respectively. LUMO derived bands were best fit by five superimposed Gaussian functions.

implies that the contributing  $C_{50}$  cages have comparatively high molecular symmetry, consistent with the formation and

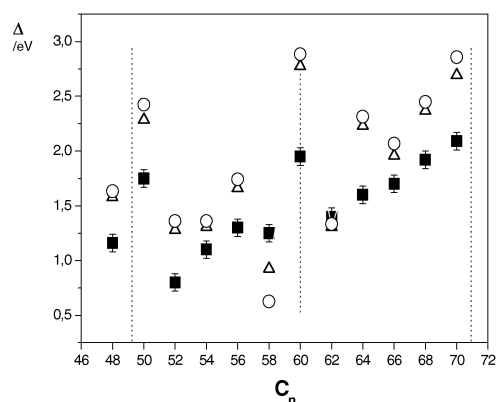


**Fig. 10** Experimentally determined HOMO-LUMO gap values,  $\Delta(n)$ , versus the number of carbon atoms per cage  $n$  (black squares). For comparison, the DFT derived  $\Delta$  values for the most stable isolated cages are also shown in<sup>49,60</sup> (open triangles). See also Table 2 which lists theoretical  $\Delta$  values of the most stable  $C_n$  isomers as well as the related mean  $\Delta^*$  values obtained for several lowest  $C_n$  isomers.

deposition of the most stable (highly symmetric) isomers as determined by DFT calculations at the B3LYP/6-31G\* level of theory. We note that the seven most stable cages (with  $D_{5h}$ ,  $D_3$ ,  $C_s$ ,  $C_2$  symmetries) are predicted to have a mean  $\Delta$  value of 1.74 eV.<sup>6</sup>

$\Delta(n)$  values have not previously been calculated for polymeric  $C_n$  solids. Hence, we can only compare measured  $\Delta$  values with the corresponding DFT-based results for isolated cages. This is illustrated in Fig. 10 which shows the experimental values versus DFT (B3LYP/6-31G\*) predictions for the lowest energy neutral  $C_n$  isomers ( $48 \leq n \leq 70$ ).<sup>62</sup> The corresponding  $\Delta(n)$  data sets appear to be highly correlated but are systematically offset from each other. The mean offset is  $\sim 0.34$  eV—likely due to in-matrix stabilization of cage-localized excess charges relative to the situation for an isolated gas-phase  $C_n$ . As in the case of the “surface ionization potentials”, the high correlation between film measurements and isolated molecule DFT- $\Delta$  calculations is rather surprising. The implication is again that the films created here by soft-landing at room temperature must consist of a considerable amount of cages with free non-IPR sites. Alternatively (or additionally), inter-cage bonds do not significantly modify the band gap relative to a hypothetical non-IPR  $C_n$  van der Waals solid. We note in closing that, in some cases, the agreement between experimental and theoretical  $\Delta(n)$  values can be further improved by also including the next most stable isomers (e.g. for  $C_{58}$ , the mean DFT- $\Delta$  value determined for the two the most stable isomers,  $C_{3v}$ : 0001 (0.91 eV) and  $C_3$ : hept (1.55 eV)<sup>51,52</sup> is in better agreement with the experimental value (1.2 eV)) (see also Table 2).

**3.3.4 X-Ray photoelectron spectroscopy.** As already shown by means of UPS, non-IPR films exhibit several distinguishing electronic markers in their valence band regions. We looked for analogous markers in C1s core states by means of XP spectroscopy. Fig. 11 shows corresponding measurements for 8 MLE-thick  $C_{60}$  and  $C_{58}$  films deposited onto  $\text{SiO}_2$  under standard conditions ( $E_{\text{kin}} \approx 6$  eV,  $T = 300$  K, surface: n-doped and oxidized Si wafer annealed under UHV).

**Table 2** Electronic parameters determined in this study for as-deposited  $C_n$  films<sup>a</sup>

Isomer (label)	Symmetry	$\Delta$ /eV Ref. 60	$\Delta^*$ /eV Ref. 49	$\Delta_{\text{exp}}$ /eV	IP/eV Ref. 64	IP*/eV	sIP <sub>exp</sub> /eV
$C_{70}$ (6000)	$D_{5h}$	2.681	2.68 (1)	2.09	7.02		6.93
$C_{68}$ (3981)	$C_2$	2.337	1.45 (11)	1.92	6.87		6.85
$C_{66}$ (1789)	$C_s$	1.951	1.62 (5)	1.70	6.86		6.65
$C_{64}$ (1998)	$D_2$	2.219	2.13 (3)	1.60	6.78		6.64
$C_{62}$ (1994)	$C_2$	1.296	1.38 (10)	1.40	6.36		6.45
$C_{60}$ (1812)	$I_h$	2.758	2.76 (1)	1.95	7.14		6.95
$C_{58}$ (1205)	$C_{3v}$	0.910	1.13 (5)	1.25	6.41	6.52 (1) Ref. 52	6.55
$C_{56}$ (916)	$D_2$	1.650	1.70 (4)	1.30	6.65		6.64
$C_{54}$ (540)	$C_{2v}$	1.311	1.43 (3)	1.10	6.61		6.70
$C_{52}$ (422)	$C_2$	1.296	1.32 (5)	0.80	6.50	6.45 (4) Ref. 63	6.85
$C_{50}$ (270)	$D_3$	2.26 (1.37)	1.85 (5)	1.75	7.26		6.95
$C_{48}$ (171)	$C_2$	1.564	1.65 (9)	1.16	6.85		6.70

<sup>a</sup> Listed are HOMO–LUMO gaps,  $\Delta_{\text{exp}}$ , and surface ionization potentials, sIP<sub>exp</sub>, in comparison to the corresponding  $\Delta$  and IP values calculated for the most stable classical non-IPR  $C_n$  isomers in gas-phase.  $\Delta^*$  and IP\* indicate the mean values obtained when taking into account all other (less stable)  $C_n$  isomers within 0.78 eV mol<sup>−1</sup> of the lowest energy forms. The overall number of different  $C_n$  isomers included is given in parentheses. Lowest energy isomers  $C_n$  are labelled according to the Fowler and Manolopoulos scheme.<sup>69</sup>

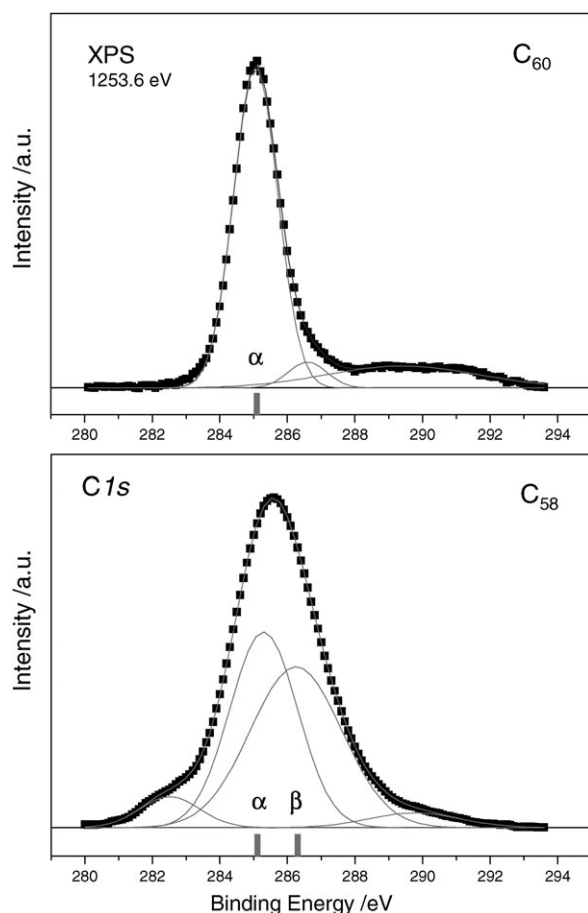


**Fig. 11** XP spectra in the C1s state regions as obtained for thick  $C_{60}$  and  $C_{58}$  films, upper and lower panels, respectively. The  $\beta$  component is present only in the XP spectra of the  $C_{58}$  film and correspondingly may be regarded as an electronic marker for (quasi covalently inter-linked) non-IPR sites.

The  $C_{60}$  XP-C1s spectrum is fully consistent with the literature.<sup>67</sup> Its main band is peaked at 285.1 eV and can be well fit by one Gaussian component,  $\alpha$ , having FWHM  $\approx$  1.6 eV. Towards

higher binding energy, weak shake-up satellites are also visible, which together form a rather broad band with two separately fitable features at  $\sim$ 286.4 eV and  $\sim$ 289.5 eV. The latter has been attributed to the decay of the low-energy plasmon.<sup>68</sup> In contrast to the  $C_{60}$  film, the main band in the  $C_{58}$  XP-C1s spectrum is significantly broader ( $\sim$ 3.1 eV) and shifted towards higher binding energy (by  $\sim$ 0.55 eV). It can be well fitted with only two components,  $\alpha$  and  $\beta$  of roughly equal intensity and separated by  $\sim$ 1.2 eV. Component  $\beta$  is peaked at 286.3 eV and does not appear in the  $C_{60}$  spectrum. The shake-up features recognizable as a separate band in the  $C_{60}$ -XP spectrum are not as clearly present in the  $C_{58}$ -XP spectrum. The  $C_{58}$ -C1s band resembles the C1s peak found for amorphous carbon films.<sup>67</sup> Both exhibit similar broadening with respect to the  $C_{60}$ -C1s peak. However, while the  $C_{58}$ -C1s band is broadened and shifted towards higher binding energies, the corresponding broad band of amorphous carbon has its maximum at the  $C_{60}$ -C1s peak position. Apparently, the  $\beta$  component in the  $C_{58}$ -C1s spectrum is a measure of non-IPR sites in the  $C_{58}$  oligomers. In future, we intend to perform systematic XPS measurements in order to explore the relation between broadening of the C1s peak and cage size.

#### 4. Summary and outlook

Mass-selective soft landing ( $E_{\text{kin}} = 6$  eV) of fragment cations generated by electron impact ionization of thermally sublimed  $C_{60}(I_h)$  and  $C_{70}(D_{5h})$  has been used to generate a new class of multilayer fullerene-nanofilms comprising classical non-IPR carbon cages ( $C_n$ ;  $48 < n < 60$  and  $60 < n < 70$ ) on HOPG. Relative to the IPR reference phases (*i.e.*  $C_{60}(I_h)$ ,  $C_{70}(D_{5h})$ ), non-IPR films show significantly (and qualitatively) different properties.

For all of the non-IPR fullerene cage sizes studied here, resultant film topographies, thermal stabilities as well as general electronic properties (VB-DOS, sIP and HOMO–LUMO gaps ( $\Delta$ )), can be rationalized in terms of the formation of covalent inter-cage bonds involving reactive non-IPR-sites (which typically comprise adjacent pentagon pairs).

Furthermore, our measurements show that the properties of non-IPR  $C_n$  films exhibit a systematic dependence on the size of the building blocks. The corresponding size dependencies found for  $E_{\text{des}}(n)$ ,  $\Delta(n)$ ,  $\text{sIP}(n)$ , can be rationalized by assuming that the non-IPR films are composed predominantly of the most stable (neutral)  $C_n$  isomers at that particular size—as predicted by density functional theory calculations. In particular, the observed decrease in  $E_{\text{des}}(n)$  with increasing size can be interpreted to first order in terms of the numbers and spatial distributions of non-IPR reaction centres on the corresponding cages. However, slight but systematic differences between the  $\text{DOS}(n)$  functions of  $[C_{70}]$ - and  $[C_{60}]$ -derived fragment families indicate that the number of these non-IPR reaction centres alone is insufficient to fully explain the electronic structure trends observed. Additionally, the cage-specific local structure and relative orientation of pentagon adjacency sites (*i.e.* C–C bond lengths and pyramidal angles) also play an important role.

In future, we will attempt to more directly determine the corresponding non-IPR isomer compositions and linkages—using a combination of scanning tunnelling microscopy, vibrational spectroscopy and diffraction measurements for molecular structure determination. This should in turn facilitate further studies of the characteristic chemical properties of non-IPR films. So far, the smallest cluster size for which we have succeeded in generating multilayer non-IPR fullerene films is  $n = 48$ . It will be of interest to develop appropriate ion sources so as to access molecularly uniform solids (or mixed/layered films) comprising even smaller all-carbon cluster building blocks. From the viewpoint of deposition dynamics, the extent of activation barriers for covalent bond formation and their influence on island growth remains to be explored. Finally, non-IPR cages deposited onto HOPG at room temperature provide a conveniently accessible and chemically well-defined model system with which to study the principles of two-dimensional fractal formation and (thermally- or reaction-induced) dissolution. In combination with appropriate surface prestructuring on the nanometer scale, a more quantitative understanding of the associated mass transport processes should facilitate novel “self-assembly” strategies of potential interest for all-carbon nanotechnology.

## Acknowledgements

This research was supported by the Deutsche Forschungsgemeinschaft (DFG) and the State of Baden-Württemberg through the DFG-Center for Functional Nanostructures (CFN) within subproject C4.6.

## References

- 1 H. W. Kroto, *Nature*, 1987, **329**, 529.
- 2 *Fullerene: Chemistry, Physics and Technology*, ed. K. M. Kadish and R. S. Ruoff, Wiley, New York, 2002.
- 3 E. Albertazzi, C. Domene, P. W. Fowler, T. G. Heine, G. Seifert, C. V. Alsenov and F. Zerbetto, *Phys. Chem. Chem. Phys.*, 1999, **1**, 2913.
- 4 P. W. Fowler, *Contemp. Phys.*, 1996, **37**, 235.
- 5 E. E. Campbell, P. W. Fowler, D. Mitchell and F. Zerbetto, *Chem. Phys. Lett.*, 1996, **250**, 544.
- 6 S. Díaz-Tendero, M. Alcamí and F. Martín, *Chem. Phys. Lett.*, 2005, **407**, 153.
- 7 H. Kietzmann, R. Rochov, G. Ganteför, W. Eberhardt, K. Vietze, G. Seifert and P. W. Fowler, *Phys. Rev. Lett.*, 1998, **81**, 5378.
- 8 H. Prinzbach, A. Weiler, P. Landenberger, F. Wahl, J. Wörth, L. T. Scott, M. Gelmont, D. Olevano and B. v. Issendorff, *Nature*, 2000, **407**, 60.
- 9 C. Piskoti, J. Yarger and A. Zettl, *Nature*, 1998, **393**, 771.
- 10 W. Krätschmer, L. D. Lamb, K. Fostiropoulos and D. R. Huffman, *Nature*, 1990, **347**, 354.
- 11 A. Koshio, M. Inakuma, T. Sugai and H. Shinohara, *J. Am. Chem. Soc.*, 2000, **122**, 398.
- 12 X. Lu, Z. Chen, W. Thiel, P. von Rague Schleyer, R. Huang and L. Zheng, *J. Am. Chem. Soc.*, 2004, **126**, 14871.
- 13 X. Gao and Y. Zhao, *J. Comput. Chem.*, 2007, **28**, 795.
- 14 Q.-Bo. Yan, Q.-R. Zheng and G. Su, *Carbon*, 2007, **45**, 1821.
- 15 T. Heine, P. W. Fowler, K. M. Rogers and G. Seifert, *J. Chem. Soc., Perkin Trans. 2*, 1999, 707.
- 16 S. Y. Xie, F. Gao, X. Lu, R. B. Huang, C. R. Wang, X. Zhang, M. L. Liu, S. L. Deng and L. S. Zheng, *Science*, 2004, **304**, 699.
- 17 C.-R. Wang, Z.-Q. Shi, L.-J. Wan, X. Lu, L. Dunsch, C.-Y. Shu, Y.-L. Tang and H. Shinohara, *J. Am. Chem. Soc.*, 2006, **128**, 6605.
- 18 Q.-B. Yan, Q.-R. Zheng and G. Su, *Carbon*, 2007, **45**, 1821.
- 19 C. R. Wang, T. Kai, T. Tomiyama, T. Yoshida, Y. Kobayashi and E. Nishibori, *Nature*, 2000, **408**, 426.
- 20 Y.-Z. Tan, S.-Y. Xie, R.-B. Huang and L.-S. Zheng, *Nat. Chem.*, 2009, **1**, 450.
- 21 Z. Q. Shi, X. Wu, C. R. Wang, X. Lu and H. Shinohara, *Angew. Chem., Int. Ed.*, 2006, **45**, 2107.
- 22 P. A. Troshin, A. G. Avent, A. D. Darwish, N. Martsinovich, A. K. Abdul-Sada, J. M. Street and R. Taylor, *Science*, 2004, **309**, 278.
- 23 W. Qian, S.-C. Chuang, R. B. Amador, T. Jarroson, M. Sander, S. Pieniazek, S. I. Khan and Y. Rubin, *J. Am. Chem. Soc.*, 2003, **125**, 2066.
- 24 M. Côté, J. C. Grossman, M. L. Cohen and S. G. Louie, *Phys. Rev. Lett.*, 1998, **81**, 697.
- 25 A. J. Du, Z. Y. Pan, Y. K. Ho, Z. Huang and Z. X. Zhang, *Phys. Rev. B: Condens. Matter*, 2002, **66**, 035405.
- 26 P. W. Fowler, T. Heine, K. M. Rogers, J. P. B. Sandall, G. Seifert and F. Zerbetto, *Chem. Phys. Lett.*, 1999, **300**, 369.
- 27 E. G. Gal'pern, I. V. Stankevich, A. L. Chistyakov and L. A. Chernozatonskii, *J. Mol. Graphics Modell.*, 2001, **19**, 189.
- 28 L. Zhechkov, T. Heine and G. Seifert, *J. Phys. Chem. A*, 2004, **108**, 11733.
- 29 V. Paillard, P. Melion, V. Dupuis, A. Perez, J. P. Perez, G. Guiraud, J. Fornazero and G. Panczer, *Phys. Rev. B: Condens. Matter*, 1994, **49**, 11433.
- 30 P. Melion, V. Paillard, V. Dupuis, A. Perez, P. Jensen, A. Hoareau, J. P. Perez, J. Tuailon, M. Broyer, J. L. Vialle, M. Pellarin, B. Bagnenard and J. Lerme, *Int. J. Mod. Phys. B*, 1995, **9**, 339.
- 31 P. Milani and S. Iannotta, *Cluster Beam Synthesis of Nanostructured Materials*, Springer, Berlin, 1999.
- 32 B. G. Levi, *Phys. Today*, 2001, **1**, 15.
- 33 A. Böttcher, P. Weis, S.-S. Jester, D. Löffler, A. Bihlmeier, W. Kloppe and M. M. Kappes, *Phys. Chem. Chem. Phys.*, 2005, **7**, 2816.
- 34 S. Matt, P. Scheier, A. Stamatovic, H. Deutsch, K. Becker and T. D. Märk, *Philos. Trans. R. Soc. London, Ser. A*, 1999, **357**, 1201.
- 35 D. Löffler, S.-S. Jester, P. Weis, A. Böttcher and M. M. Kappes, *J. Chem. Phys.*, 2006, **124**, 054705.
- 36 Z. Y. Li, *Surf. Sci.*, 1999, **441**, 366.
- 37 P. A. Gravi, M. Devel, Ph. Lambin, X. Bouju, Ch. Girard and A. A. Lucas, *Phys. Rev. B: Condens. Matter*, 1996, **53**, 1622.
- 38 D. J. Kenny and R. E. Palmer, *Surf. Sci.*, 2000, **447**, 126.
- 39 H. Liu and P. J. Reinke, *J. Chem. Phys.*, 2006, **124**, 164707.
- 40 V. Liu, Z. Lin, L. V. Zhigilei and P. Reinke, *J. Phys. Chem. C*, 2008, **112**, 4687.
- 41 S. Yao, C. Zhou, B. Han, T. Fan, J. Wu, L. Chen and H. Cheng, *Phys. Rev. B: Condens. Matter*, 2009, **79**, 155304.
- 42 Y. Miyamoto and M. Saito, *Phys. Rev. B: Condens. Matter*, 2001, **63**, 161401.
- 43 S.-S. Jester, D. Löffler, P. Weis, A. Böttcher and M. M. Kappes, *Surf. Sci.*, 2009, **603**, 1863.
- 44 A. Bihlmeier, C. C. M. Samson and W. Kloppe, *ChemPhysChem*, 2005, **6**, 2625.



- 45 (a) I.-H. Lee, *et al.*, *Appl. Phys. Lett.*, 2006, **88**, 011913;  
 (b) S. Bando, T. Hiraoka, T. Yumura, K. Hirahara, H. Shinohara and S. Iijima, *Chem. Phys. Lett.*, 2004, **384**, 320.
- 46 P. A. Redhead, *Vacuum*, 1962, **12**, 203.
- 47 X. Lu and Z. Chen, *Chem. Rev.*, 2005, **105**, 3643.
- 48 Note that in the initial deposition stages only surface defects and step edges are decorated by  $C_n$  cages (even for very gentle deposition conditions,  $E_{\text{kin}} < 1 \text{ eV}^{33,35}$ ). This indicates that non-IPR cage-HOPG binding is insignificant by comparison.
- 49 N. Shao, Y. Gao and X. C. Zeng, *J. Phys. Chem. C*, 2007, **111**, 17671.
- 50 S. Diaz-Tendero, M. Alcamí and F. Martin, *J. Chem. Phys.*, 2003, **119**, 5545.
- 51 D.-L. Chen, W. Q. Tian, J.-K. Feng and C.-C. Sun, *ChemPhysChem*, 2008, **9**, 454.
- 52 D.-L. Chen, W. Q. Tian, J.-K. Feng and C.-C. Sun, *ChemPhysChem*, 2007, **8**, 1029.
- 53 Note that this remains true even when considering the second most stable neutral isomers:  $C_{68}$  [ $C_2$ : 0178] and  $C_{58}$  [ $C_5$ : *hept*] which would be present in a hot neutral beam ( $T_B < 1000 \text{ K}$ ) at relative concentrations of less than 38% and 9%, respectively<sup>51,52</sup>.
- 54 D. Löffler, *et al.*, in preparation.
- 55 H. Ulbricht, G. Moos and T. Hertel, *Phys. Rev. Lett.*, 2003, **90**, 095501.
- 56 The  $m(n)$  values were obtained by averaging the theoretical values predicted for the most stable  $C_n^{(0)}$  and  $C_n^{(+)}$  cages. In the case of  $C_{62}$  the presence of a heptagonal ring has been ignored by taking into account the 3-2AP motifs only.
- 57 S. Ulas, *et al.*, in preparation.
- 58 (a) P. He, S. Bao, C. Yu and Y. Xu, *Surf. Sci.*, 1995, **328**, 287;  
 (b) S. He, M. Arita, H. Namatame, M. Taniguchi, H.-N. Li and H.-Y. Li, *J. Phys.: Condens. Matter*, 2007, **19**, 026202;  
 (c) M. Knupfer, D. M. Poirier and J. H. Weaver, *Phys. Rev. B: Condens. Matter*, 1994, **49**, 2284.
- 59 Expanded scale segments are shown following background subtraction. For this, a function  $A\exp(E_{\text{bind}}/B)$  has been fitted in the spectral region between  $E_{\text{bind}} = 0$  and first minimum at binding energy  $\sim 4 \text{ eV}$ .
- 60 M. Alcamí, G. Sanches, S. Diaz-Tendero, Y. Wang and F. Martin, *J. Nanosci. Nanotechnol.*, 2007, **7**, 1329.
- 61 O. Boltalina, I. N. Ioffe, L. N. Sidorov, G. Seifert and K. Vietze, *J. Am. Chem. Soc.*, 2000, **122**, 9745.
- 62 In order to apply the same fit procedure to the HOMO-bands of all members of both  $[C_{60}]$  and  $[C_{70}]$  families we repeated the measurements of  $C_{58}$ ,  $C_{56}$ ,  $C_{54}$ , and  $C_{52}$  films. Whereas the  $\text{IP}(C_n)$  values well reproduce those presented in ref. 35 the new  $\text{IP}(C_{52})$  value differs significantly. The error in our old  $\text{IP}(C_{52})$  value was traced to an error in pinning the referencing Fermi level.
- 63 S. Diaz-Tendero, F. Martin and M. Alcamí, *ChemPhysChem*, 2005, **6**, 92.
- 64 S. Diaz-Tendero, G. Sánchez, M. Alcamí and F. Martin, *Int. J. Mass Spectrom.*, 2006, **252**, 133.
- 65 J. A. Zimmerman, J. R. Eyler, S. B. H. Bach and S. W. McElvany, *J. Chem. Phys.*, 1991, **94**, 3556.
- 66 D. Löffler, N. Bajales, M. Cudaj, P. Weis, S. Lebedkin, A. Bihlmeier, D. P. Tew, W. Klopper, A. Böttcher and M. M. Kappes, *J. Chem. Phys.*, 2009, **130**, 164705.
- 67 J. A. Leiro, M. H. Heinonen, T. Laihoa and I. G. Batirev, *J. Electron Spectrosc. Relat. Phenom.*, 2003, **128**, 205.
- 68 M. Ramm, M. Ata, K.-W. Brzezinka, T. Gross and W. Unger, *Thin Solid Films*, 1999, **354**, 106.
- 69 P. W. Fowler and D. E. Manolopoulos, *An Atlas of Fullerenes*, Clarendon, Oxford, UK, 1995.